ARTICLE OPEN

Check for updates

Chiral superconductivity with enhanced quantized Hall responses in moiré transition metal dichalcogenides

Michael M. Scherer[1,2]✉, Dante M. Kennes[3,4] and Laura Classen[5,6]

Experimental demonstrations of tunable correlation effects in magic-angle twisted bilayer graphene have put two-dimensional moiré quantum materials at the forefront of condensed-matter research. Other twisted few-layer graphitic structures, boron-nitride, and homo- or hetero-stacks of transition metal dichalcogenides (TMDs) have further enriched the opportunities for analysis and utilization of correlations in these systems. Recent experiments within the latter material class confirmed the relevance of many-body interactions and demonstrated the importance of their extended range. Since the interaction, its range, and the filling can be tuned experimentally by twist angle, substrate engineering and gating, we here explore Fermi surface instabilities and resulting phases of matter of hetero-bilayer TMDs. Using an unbiased renormalization group approach, we establish in particular that hetero-bilayer TMDs are platforms to realize topological superconductivity with winding number $|\mathcal{N}| = 4$. We show that this state reflects in pronounced experimental signatures, such as distinct quantum Hall features.

npj Quantum Materials (2022)7:100 ; https://doi.org/10.1038/s41535-022-00504-z

INTRODUCTION

The pairing of electrons in a superconductor is among the most intriguing effects in the study of collective phenomena. One strong driving force in the exploration of superconductors is the quest for ever higher critical temperatures[1,2] close to ambient conditions with numerous high impact technological applications. So far the highest critical temperatures were either achieved in conventional, BCS-like superconductors but only under the application of immense pressure (with critical temperatures reaching room temperature) or at ambient pressure via an unconventional superconducting pairing mechanism[3] (with critical temperatures reaching approximately 100 K). Developing a deepened understanding of the latter, raising the hope to relief the high pressure condition, is thus of utmost importance. At the same time, combining superconductivity with non-trivial topology is a promising route for quantum information sciences as such topological superconductors may harbor robust edge states at domain boundaries with topological properties advantageous to computing applications[4].

However, realizing and controlling topological superconductors proves difficult to this date, with only a few candidate materials currently being suggested, e.g.,[5–9]. A new direction in the study of superconductivity opened up recently in twisted moiré quantum materials, i.e. two-dimensional van der Waals materials being stacked at a relative twist angle[10–28]. In these systems kinetic energy scales can be tuned by the twist angle allowing to promote the relative relevance of potential, spin-orbit coupling or other energy scales[17]. Indeed, topological properties as well as superconductivity were already demonstrated in these highly versatile systems and as a consequence they could provide an excellent opportunity to engineer topological superconductors. In particular, in moiré transition metal dichalcogenides, strong spin-orbit coupling or excitonic physics were experimentally explored. The observation of a Mott insulating state[29,30] and other fascinating collective phenomena such as generalized Wigner crystals[30], stripe phases[31] and quantum anomalous Hall insulators[32] confirmed the relevance of many-body interactions, and demonstrated the importance of their extended range. Moreover, near the insulating state, indications of superconductivity were found in homobilayer twisted WSe_2[33].

Here, we explore this idea for moiré transition metal dichalcogenides (see Fig. 1a)[17,29,33–42] by analyzing the Fermi surface instabilities of twisted hetero-bilayers of WX_2/MoX'_2 (X,X′ = S,Se) away from half filling of the moiré band. We unveil an exotic superconducting state near Van Hove filling described by form factors with eight zero crossings, arising from the extended range of interactions in these materials. We show that the superconducting ground state is formed by a chiral configuration, which is characterized by a full gap on the Fermi surface and non-trivial topology with winding number $|\mathcal{N}| = 4$. We argue that this type of topological superconductivity leads to distinct experimental signatures in quantum Hall transport measurements and elevates twisted hetero-bilayers of TMDs to prime candidates for experimental scrutiny of topological superconductivity.

In a range of small twist angles, isolated and narrow moiré bands emerge in TMD hetero-bilayers of WX_2/MoX'_2 (X,X′ = S,Se)[33–39]. These flat bands are formed by the highest, spin-polarized valence band of WX_2 and can be described by an extended triangular-lattice Hubbard model $H = H_0 + H_I$, which features an effective SU(2) valley symmetry[34]

$$H_0 = \sum_{\nu=\pm}\left[\sum_{ij} t_{i-j} c^\dagger_{i,\nu} c_{j,\nu} - \mu \sum_i c^\dagger_{i,\nu} c_{i,\nu}\right] \tag{1}$$

$$H_I = U \sum_i n_{i,+} n_{i,-} + \sum_{ij} V_{i-j} n_i n_j. \tag{2}$$

[1]Institut für Theoretische Physik III, Ruhr-Universität Bochum, 44801 Bochum, Germany. [2]Institut für Theoretische Physik, Universität zu Köln, 50937 Cologne, Germany. [3]Institute for Theory of Statistical Physics, RWTH Aachen University, and JARA Fundamentals of Future Information Technology, 52056 Aachen, Germany. [4]Max Planck Institute for the Structure and Dynamics of Matter, Center for Free Electron Laser Science, Luruper Chaussee 149, 22761 Hamburg, Germany. [5]Condensed Matter Physics & Materials Science Division, Brookhaven National Laboratory, Upton, NY 11973-5000, USA. [6]Max Planck Institute for Solid State Research, Heisenberg Str. 1, 70569 Stuttgart, Germany. ✉email: scherer@tp3.rub.de

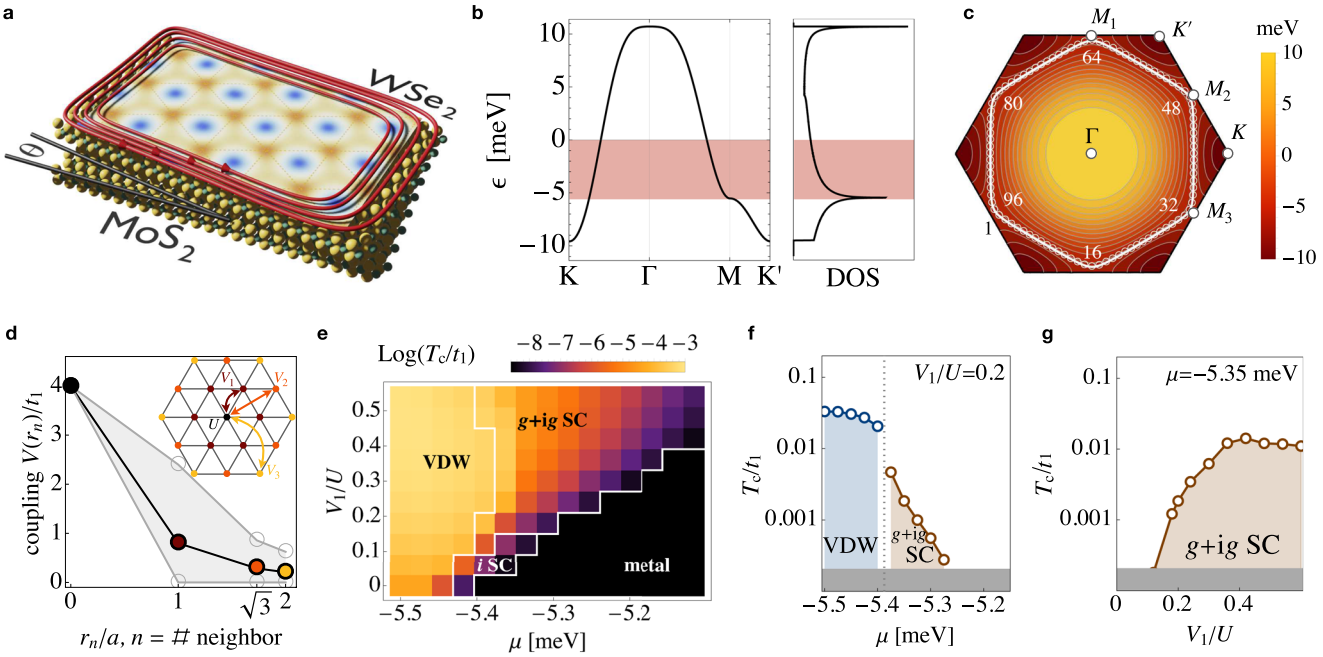

Fig. 1 Correlated phase diagram of hetero-bilayer TMDs. a Sketch of a twisted WSe_2/MoS_2 bilayer with small twist angle θ. The resulting effective moiré potential[34,39] is indicated by the contour shading at the top. The four red lines represent the chiral edge modes of the topological superconducting state with $\mathcal{N}=4$. **b** Dispersion of the energy band $\epsilon_{\mathbf{k}}$ along high-symmetry lines and density of states (DOS). We explore filling levels indicated by the red band between half filling ($\mu\sim 0$) and Van Hove filling ($\mu=-5.5$ meV, ~1/4 filling). **c** Nearly nested Fermi surface close to the Van Hove energy. Numbered open circles show the momentum resolution of the Fermi surface employed in the FRG approach. **d** Extended interaction parameters as function of distance r_n/a, a is the moiré lattice spacing[34,39]. The gray area marks the explored range of interactions, which are tunable by the environment. Inset: sketch of the interactions on the triangular moiré lattice. **e** Phase diagram as function of nearest-neighbor repulsion V_1 and filling controlled by the chemical potential μ extracted from the Fermi-liquid instabilities in the FRG flow for $U=4t_1$, $V_2/V_1=0.357$ and $V_3/V_1=0.260$ (see Fig. 1d). The background color encodes our estimate for the critical temperature (see methods). We find an instability towards a valley density wave (VDW) near Van Hove filling $\mu\approx -5.5$ meV. It is flanked by an i-wave superconducting instability (iSC) for small V_1/U and by a g-wave superconducting instability for larger V_1/U. In the ground state, the g-wave superconducting instability forms a chiral $g+ig$ state ($g+ig$ SC) characterized by winding number $\mathcal{N}=4$. The regime colored in black, does not show any instability within our numerical accuracy. **f** Filling-dependent critical temperature near Van Hove filling. Below the gray band, we cannot resolve any instability within our numerical accuracy. **g** Dependence of the critical temperature on the extended interactions tuned via V_1/U at fixed V_2/V_1, V_3/V_1 slightly away from Van Hove filling.

Here, $n_i=\sum_\nu n_{i,\nu}$ and $n_{i,\nu}=c^\dagger_{i,\nu}c_{i,\nu}$ is the number of electrons on site i with valley index $\pm$, $c^{(\dagger)}_{i,\nu}$ are the corresponding annihilation (creation) operators. Ref. [34] derived this model for $WSe_2/MoSe_2$ and for WSe_2/MoS_2 with R- and H-stacking configurations. The hopping amplitudes t_n for the nth-nearest neighbors depend on the twist angle and we consider typical values for vanishingly small twist angle $t_1\approx 2.5$ meV, $t_2\approx -0.5$ meV, $t_3\approx -0.25$ meV[34]. The resulting moiré band $\epsilon_{\mathbf{k}}$ features a Van Hove peak in the density of states near 1/4 filling (−5.5 meV), where the Fermi surface is approximately nested (Fig. 1b, c). In experiment, the filling can be adjusted, and Van Hove filling can be reached, by tuning the gate voltage, which we model here by varying the chemical potential μ between 1/4 and 1/2 filling. The interaction parameters U, V_n also depend on the twist angle, and on the dielectric environment so that the strength and range of interactions can be controlled[43]. First-principles calculations show that the extended interactions V_n are sizable in effective models for hetero-bilayer TMDs[34]. For our analysis, we use an intermediate interaction strength for the onsite interaction $U=4t_1$ and explore the effect of further-ranged interactions by varying $V_1/U\in[0, 0.5]$ with $V_2/V_1\approx 0.357$ and $V_3/V_1\approx 0.260$[34,39] (Fig. 1d, $V_{n\geq 4}=0$). In a second step we also investigate the impact of an additional nearest-neighbor exchange interaction $H_J=J\sum_{\langle i,j\rangle}\mathbf{S}_i\mathbf{S}_j$ to model strong-coupling effects.

RESULTS

Correlated phase diagram

We study the correlated phases of hetero-bilayer TMDs that emerge out of a metallic state within an itinerant scenario using the fermionic functional renormalization group (FRG)[44,45]. This method has been successfully applied to scenarios which aim at a realistic modeling of various materials, see, e.g.[46–48] for some recent contributions or the review[49] for a more exhaustive list of references. The FRG resolves the competition between different ordering tendencies in an unbiased way and is employed to calculate the dressed, irreducible two-particle correlation function $V(\mathbf{k}_1,\mathbf{k}_2,\mathbf{k}_3,\mathbf{k}_4)$ for electrons with momenta $\mathbf{k}_i$, $i=1\ldots4$, on the Fermi surface (Fig. 1c). It is valley-independent due to the SU(2) valley symmetry (see Methods). Upon lowering the temperature, $V(\mathbf{k}_1,\mathbf{k}_2,\mathbf{k}_3,\mathbf{k}_4)$ develops sharp, localized peaks for characteristic momentum combinations, indicating long-ranged correlations in real space. This allows us to extract the temperature where a strongly-correlated state forms, as well as the symmetry and type of the strongest correlations (see Methods).

In our model for hetero-bilayer TMD moiré systems, instabilities near 1/4 filling occur due to the high density of states and approximate nesting, which leads to symmetry-broken ground states. We start with varying μ and V_n and calculate the phase diagram based on the two-particle correlation functions (Fig. 1e).

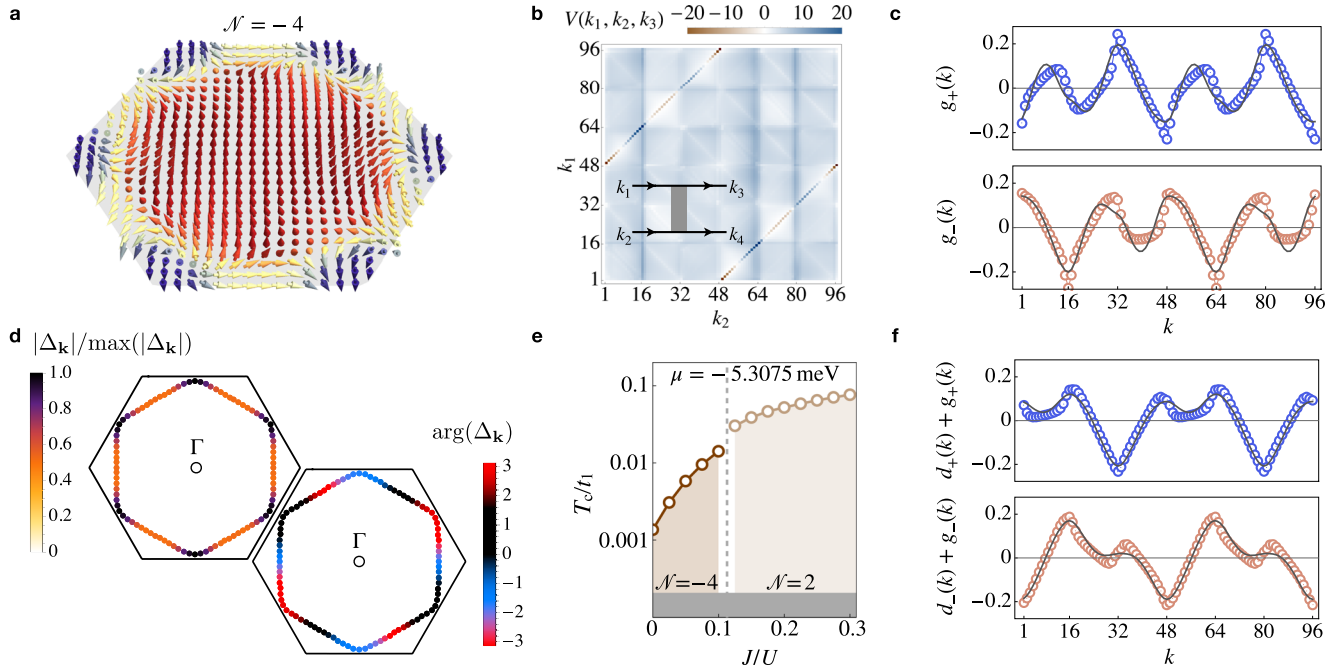

Fig. 2 Topological superconductivity in hetero-bilayer TMDs. a The phase winding of the superconducting gap in the $g + ig$ state can be visualized by a skyrmion configuration constructed from the vector $\mathbf{m} = (\mathrm{Re}\Delta_\mathbf{k}, \mathrm{Im}\Delta_\mathbf{k}, \xi_\mathbf{k})/(\xi_\mathbf{k}^2 + |\Delta_\mathbf{k}|^2)^{1/2}$. $\mathbf{m}$ points up (down) at the highest (lowest) energies $\xi_\mathbf{k} = \epsilon_\mathbf{k} - \mu$ and rotates $\mathcal{N}$ times in the plane in the vicinity of the Fermi level $\xi_\mathbf{k} = 0$. The skyrmion configuration is used to calculate the winding number $\mathcal{N}$, which for a broad range of fillings around Van Hove filling is $|\mathcal{N}| = 4$, indicating an enhanced response in thermal and spin quantum Hall measurements. **b** Functional RG data of the irreducible two-particle correlation function $V(\mathbf{k}_1, \mathbf{k}_2, \mathbf{k}_3, \mathbf{k}_4)$ near the instability temperature for incoming wave vectors $\mathbf{k}_1, \mathbf{k}_2$. Wave vectors are labeled by the patch points along the Fermi surface indicated in Fig. 1c. The outgoing wave vector $\mathbf{k}_3$ is fixed at patch no. 1 and $\mathbf{k}_4 = \mathbf{k}_1 + \mathbf{k}_2 - \mathbf{k}_3$ is given by momentum conservation. The sharp diagonal features occur at $\mathbf{k}_1 = -\mathbf{k}_2$, $\mathbf{k}_3 = -\mathbf{k}_4$, indicating the formation of long-ranged superconducting correlations. **c** Superconducting form factors $g_\pm(k)$ extracted from $V(\mathbf{k}_1, \mathbf{k}_2, \mathbf{k}_3, \mathbf{k}_4)$ in b. They exhibit a large overlap with a linear combination of the second-nearest-neighbor lattice harmonics $g_1(\mathbf{k}), g_2(\mathbf{k})$ (solid gray lines) defined in the text, which belong to the two-dimensional irreducible representation E_2 of the lattice symmetry group C_{6v}. We classify them as g-wave form factors due to their eight nodes. **d** Absolute value and phase of the gap function on the Fermi surface. The chiral superposition $\Delta_\mathbf{k} = |\Delta|(g_1(\mathbf{k}) \pm ig_2(\mathbf{k}))$ fully gaps the Fermi surface, thereby minimizing the energy. Such a $g + ig$ superconducting state breaks time-reversal symmetry and is topological with a four-fold phase winding along the Fermi surface $|\mathcal{N}| = 4$. **e** Stability of the g-wave superconduting state towards inclusion of J/U for $V_1/U = 0.2$ at $\mu = 5.3075$ meV. For growing values of the exchange interaction J, the nearest-neighbor harmonics d_1 and d_2 of E_2 (defined in the text) start to contribute as indicated by the colored transition. They are pure d-wave form factors with only four nodes. For $J/U \lesssim 0.1$, the contribution from d_1 and d_2 is negligible. **f** Example of the extracted form factors for $J/U = 0.5$ where d_1, d_2 and g_1, g_2 roughly contribute by equal amounts, showing the change in the number of nodes due to the admixture.

Closest to Van Hove filling $\mu \approx -5.5$ meV, we find that correlations corresponding to a valley density wave (VDW) are strongest, which manifest themselves by peaks at the nesting momenta $\mathbf{Q}_\alpha$, $\alpha = 1, 2, 3$ in $V(\mathbf{k}_1, \mathbf{k}_2, \mathbf{k}_3, \mathbf{k}_4)$, i.e. at $\mathbf{k}_3 - \mathbf{k}_1 = \mathbf{Q}_\alpha$ or $\mathbf{k}_3 - \mathbf{k}_2 = \mathbf{Q}_\alpha$. This state is the analogue of a spin density wave[50,51] considering that, here, the SU(2) symmetry belongs to a pseudo-spin formed by the valleys. The VDW instability is insensitive towards the inclusion of V_n in the explored range.

Moving the filling slightly away from Van Hove filling, we obtain a superconducting instability, which is indicated by diagonal peak positions, i.e. $V(\mathbf{k}_1, \mathbf{k}_2, \mathbf{k}_3, \mathbf{k}_4) \approx V(\mathbf{k}_1, -\mathbf{k}_1, \mathbf{k}_3, -\mathbf{k}_3)$, that correspond to electron pairs with a total momentum of zero $\mathbf{k}_1 + \mathbf{k}_2 = \mathbf{k}_3 + \mathbf{k}_4 = \mathbf{0}$ (Fig. 2b). Increasing the filling further reduces the critical temperature until it vanishes (Fig. 1f). Its origin lies in the strong particle-hole fluctuations due to nesting, which induce an attraction in the pairing channel (see Methods). The inclusion of V_n has a profound impact: it strongly affects the symmetry of the superconducting correlations, because it penalizes electrons to be simultaneously on neighboring sites, so that electron pairing is shifted to farther-distanced neighbors. As a result, the largest attraction is promoted to occur in a higher-harmonic channel.

The symmetry of the pair correlations can be classified in terms of the irreducible representations of the lattice point group C_{6v} by expanding the eigenfunctions of $V(\mathbf{k}, -\mathbf{k}, \mathbf{k}', -\mathbf{k}')$ in lattice harmonics. Within an irreducible representation, lattice harmonics with the same symmetry but different angular-momentum form factors can mix and it depends on microscopic details which lattice harmonics are the strongest. The valley symmetry follows from the properties of the lattice harmonics under inversion: even (odd) lattice harmonics correspond to valley singlet (triplet) pairing. We obtain two valley-singlet pairing regimes with different spatial symmetries depending on V_n. For small V_n, we find a small regime with A_2 symmetry (i-wave) in agreement with previous results for $V_n = 0$[52,53]. However, for larger V_n ($V_1/U \gtrsim 0.15$), including realistic values in twisted TMDs[34,39], we unveil a large regime with E_2 symmetry, which contains both, d- and g-wave form factors. The pair correlations in this regime are fitted well using the second-nearest-neighbor lattice harmonics $g_1(\mathbf{k}) = 8/9[-\cos(3k_x/2)\cos(\sqrt{3}k_y/2) + \cos(\sqrt{3}k_y)]$, $g_2(\mathbf{k}) = 8/(3\sqrt{3})\sin(3k_x/2)\sin(\sqrt{3}k_y/2)$ (Fig. 2c). We can categorize them as g-wave based on their eight nodes and we note that the number of nodes on the Fermi surface depends on the chemical potential. It is four if the Fermi surface is closer to Γ (where we do not find a superconducting instability), and eight near Van Hove energy (where we do find one). The eight nodes are favored over the nearest-neighbor (d-wave) harmonics with four nodes due to the strong bare nearest-neighbor repulsion. That V_1 drives this instability can also be seen at the critical temperature,

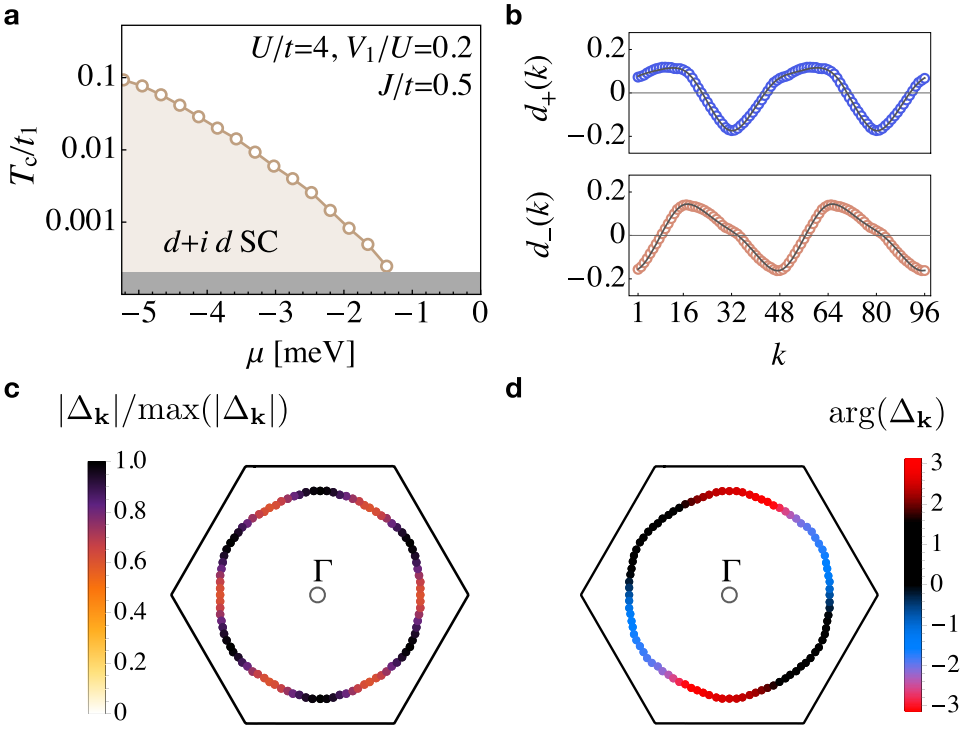

Fig. 3 Effect of exchange coupling. a Filling-dependent critical temperature for a sizable exchange coupling $J/t = 0.5$. The exchange coupling generates a d-wave instability, which indicates a chiral $d + id$ ground state. **b** Superconducting form factors $d_\pm(k)$ extracted from $V(\mathbf{k}_1, \mathbf{k}_2, \mathbf{k}_3, \mathbf{k}_4)$ which exhibit a large overlap with a linear combination of nearest-neighbor lattice harmonics d_1, d_2 (solid gray lines) defined in the text. Their chiral superposition $d \pm id$ fully gaps the Fermi surface with the gap function $\Delta(k)$ shown in the lowest panels (**c**, **d**). The phase winds twice around the Fermi surface.

which initially increases with V_1 and then saturates (see Fig. 1g). The selection of the higher lattice harmonics due to V_1 has measurable consequences for the topological properties of the superconducting state.

Chiral superconductivity and quantized Hall responses

Due to the two-dimensional E_2 symmetry, the superconducting gap has two components Δ_1, Δ_2 and additional symmetries besides $U(1)$ can be broken depending on the configuration that forms the ground state[54]. The ground-state configuration is determined by minimizing the Landau energy functional

$$\mathcal{L} = \alpha(|\Delta_1|^2 + |\Delta_2|^2) + \beta(|\Delta_1|^2 + |\Delta_2|^2)^2 + \gamma|\Delta_1^2 + \Delta_2^2|^2. \quad (3)$$

We use our FRG results as an input for the effective interaction $V(\mathbf{k}, -\mathbf{k}, \mathbf{k}', -\mathbf{k}')c^\dagger_{\mathbf{k}',\nu}c^\dagger_{-\mathbf{k}',\nu'}c_{-\mathbf{k},\nu'}c_{k,\nu}$ close to the instability and perform a Hubbard-Stratonovich transformation to describe the coupling between electrons and pairing fields $H_\mathrm{P} = \Delta_1^*(\mathbf{q})g_1(\mathbf{k})c_{\mathbf{k}+\mathbf{q},+}c_{-\mathbf{k},-} + \Delta_2^*(\mathbf{q})g_2(\mathbf{k})c_{\mathbf{k}+\mathbf{q},+}c_{-\mathbf{k},-} +$ c.c. Integrating out the electrons, we find in particular $\gamma > 0$. Thus, the chiral configuration $\Delta_1 = \mathrm{i}\Delta_2$ minimizes the energy. Such a "$g + ig$" superconducting state breaks time-reversal symmetry and is topologically non-trivial. The Fermi surface is fully gapped as we can see from the quasiparticle energy $E_\mathbf{k} = (\xi_\mathbf{k}^2 + |\Delta_\mathbf{k}|^2)^{1/2}$, where $\xi_\mathbf{k} = \epsilon_\mathbf{k} - \mu$, $\Delta_\mathbf{k} = \Delta[g_1(\mathbf{k}) + \mathrm{i}g_2(\mathbf{k})]$, and g_1, g_2 are the FRG-extracted form factors (see Fig. 2c, d). In the superconducting gap $\Delta_\mathbf{k}$, an overall trivial phase of $\Delta \in \mathbb{C}$ can be removed, in contrast to the relative phase difference of $\pi/2$ between g_1 and g_2.

The topological properties can be classified by an integer invariant based on the Skyrmion number[55–57]

$$\mathcal{N} = \frac{1}{4\pi}\int_{\mathrm{BZ}} d^2k\, \mathbf{m}\cdot\left(\frac{\partial\mathbf{m}}{\partial k_x}\times\frac{\partial\mathbf{m}}{\partial k_y}\right), \quad (4)$$

where the pseudo-spin vector is given by $\mathbf{m} = (\mathrm{Re}\Delta_\mathbf{k}, \mathrm{Im}\Delta_\mathbf{k}, \xi_\mathbf{k})/E_\mathbf{k}$. The integral over the Brillouin zone is non-zero because $\mathbf{m}$ follows the phase winding of the superconducting gap around the Fermi surface (Fig. 2a). We calculate $\mathcal{N}$ for the entire range of fillings and find $|\mathcal{N}| = 4$ in the relevant regime where the superconducting instability occurs. Importantly, the high winding number $|\mathcal{N}| = 4$ implies stronger experimental signatures compared to other topological superconductors. Four chiral edge modes appear (as illustrated in Fig. 1a) and the quantized thermal and spin response is enhanced with the spin Hall conductance given by $\sigma^s_{xy} = \mathcal{N}\hbar/(8\pi)$ and the thermal Hall conductance by $\kappa = \mathcal{N}\pi k_B 3^2/(6\hbar)$[58,59].

The $g + ig$ pairing state is robust with respect to the inclusion of small to intermediate nearest-neighbor exchange J. For example, for $V_1/U = 0.2$ and $\mu \approx -5.31$ meV, $g + ig$ pairing is dominant up to reasonably large values of $J \approx 0.1$ (Fig. 2e). For larger values of J, d-wave contributions from the nearest-neighbor form factors $d_1(\mathbf{k}) = 2(\cos k_x - \cos(k_x/2)\cos(\sqrt{3}k_y/2))$ and $d_2(\mathbf{k}) = 3/\sqrt{3}\sin(k_x/2)\sin(\sqrt{3}k_y/2)$ start to mix with the previous g-wave ones g_1, g_2 (see Fig. 2e, f). This is expected when the attraction mediated by antiferromagnetic fluctuations from J overcomes the repulsion from V_n. For larger values of J and farther away from Van Hove filling, the d-wave form factors dominate (see Fig. 3a, b). Then, the superconducting ground state is a fully gapped $d + id$ state with $|\mathcal{N}| = 2$, which can be seen from the phase of the superconducting state winding two times along the Fermi surface (see Fig. 3c, d).

DISCUSSION

Most numerical calculations in our work have been carried out for tight-binding and interaction parameters as explicitly suggested for the untwisted WSe_2/MoS_2 moiré system. However, our calculations with varied parameters suggest that the the

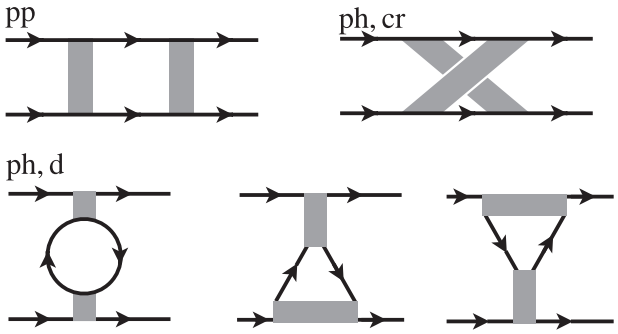

Fig. 4 Loop diagrams. Contributing to the functional RG flow, cf. Eq. (5).

correlated phase diagram is very similar in related systems that can be described by an extended Hubbard model on the triangular lattice with sizable longer-ranged density-density interactions near van Hove filling. Our results highlight twisted hetero-bilayers of TMDs as prime candidates for exotic topological superconducting states in two-dimensional materials. They allow — by moiré or substrate engineering — for a very high level of external control[17] and our identification of topological $g+ig$ superconductivity opens up pathways to interrogate this elusive phase of matter in a highly tunable setup. Exploiting the unparalleled level of control, these platforms provide the opportunity to scrutinize topological phase transitions using gating which, as we showed, drives the $g+ig$ state into a density wave or a metallic state at either side of the topological superconductor. This can also shed light on related questions about chiral superconductivity in Van-Hove-doped graphene[60–63] or about topological transitions, e.g., the nodal structure at the transition point from $|\mathcal{N}|=2$ to $|\mathcal{N}|=4$, which is intensely debated for Na_xCoO_2[64,65].

An intriguing avenue of future research concerns the relevance of disorder and finite size effects onto the *g*-wave superconducting state as moiré materials tend to form localized dislocations[66]. Similar to the $d+id$ state, we expect the $g+ig$ state to be robust against non-magnetic disorder[67,68]. However, twist-angle disorder can suppress the superconducting state and might be the reason why a clear observation of superconductivity is so far elusive in moiré TMDs (see however[33]). Another important pragmatic issue is the relevance of relaxation[69,70]. Here, we primarily investigated model parameters relevant to different-chalcogen heterobilayers, e.g., untwisted WSe_2/MoS_2, where the modeling of the moiré potential seems to be robust in comparison with experimental observations[34,71]. The description of the material as an effective triangular lattice Hubbard model should be valid even for other material combinations, but nevertheless it will be very interesting to consider the effects of lattice reconstruction, e.g., in untwisted WSe_2/MoS_2, and determine how the model parameters are tuned quantitatively in detail in future work.

From a theoretical angle, the recently developed real-space extension of the unbiased renormalization scheme used here might provide insights into these questions as well as clarify the relevance of physical boundaries[72]. Another interesting possibility is to investigate if non-local Coulomb interactions can also induce topological triplet superconductivity as discussed for ref. [47]. Substrate engineering in the field of two-dimensional systems in general and tunable moiré materials in particular is another fascinating route to follow. Building on our work (highlighting the relevance of long-ranged interactions for exotic collective phases of matter) it will be interesting to generalize the analysis to substrates allowing to engineer long-ranged, logarithmic

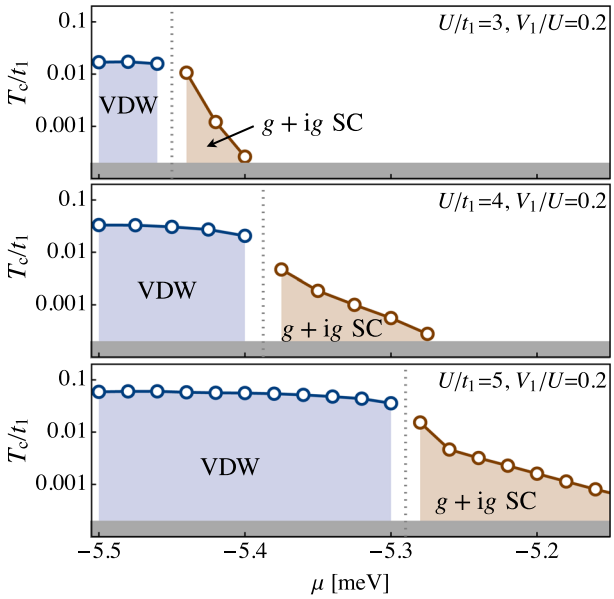

Fig. 5 *U* dependence. Critical temperature for three values of the on-site interaction U and fixed V_n. The valley density wave (VDW) and g-wave pairing phase ($g+ig$) appear near Van Hove filling in all three cases.

Keldysh-type of interactions[73] and scrutinize their effects on collective phases of matter in moiré materials.

Experimentally, Andreev reflection[74] and Raman scattering[75] provide way to distinguish the fully gapped chiral from an *s*-wave superconductor. The prediction of $g+ig$ topological superconductivity can also be verified using thermal or spin quantum Hall measurements which reveals the four-fold nature of the chiral and topologically protected edge modes. Domain walls between $\mathcal{N}=+4$ and -4 configurations must host eight propagating chiral modes[55]. Whether these edge modes can be utilized for future quantum information technologies requires additional investigation[67]. The option appears particularly intriguing with twisted hetero-bilayers of TMDs being so highly tunable and the energy scales on which the material properties can be altered being so low due to the flat bands.

METHODS

Functional renormalization group approach

We have employed the functional renormalization group method to explore the phase diagram of our model[44,45,49]. Within the FRG, we choose the temperature as the flow parameter and use an approximation that neglects feed-back from the self-energy and three-particle vertices or higher. In this approximation, we obtain a renormalization group equation for the two-particle correlation function $\Gamma^{(2p)}$ that describes its evolution upon lowering the temperature. In an SU(2)-symmetric system, $\Gamma^{(2p)}$ can be expressed via a (pseudo-)spin-independent coupling function V as $\Gamma^{(2p)}_{s_1s_2s_3s_4}(\mathbf{k}_1,\mathbf{k}_2,\mathbf{k}_3,\mathbf{k}_4)=V(\mathbf{k}_1,\mathbf{k}_2,\mathbf{k}_3,\mathbf{k}_4)\delta_{s_1s_3}\delta_{s_2s_4}-V(\mathbf{k}_1,\mathbf{k}_2,\mathbf{k}_4,\mathbf{k}_3)\delta_{s_1s_4}\delta_{s_2s_3}$, where s_i labels the (pseudo-)spin here given by the valley, and $\mathbf{k}_1$, $\mathbf{k}_2$ are incoming and $\mathbf{k}_3$, $\mathbf{k}_4$ outgoing momenta. Momentum conservation requires $\mathbf{k}_1+\mathbf{k}_2=\mathbf{k}_3+\mathbf{k}_4$, so for brevity we will use $V(\mathbf{k}_1, \mathbf{k}_2, \mathbf{k}_3)=V(\mathbf{k}_1, \mathbf{k}_2, \mathbf{k}_3, \mathbf{k}_1+\mathbf{k}_2-\mathbf{k}_3)$ in the following.

The RG equation for the temperature evolution of $V(\mathbf{k}_1, \mathbf{k}_2, \mathbf{k}_3)$ can then be written as

$$\frac{d}{dT}V=\tau_{\mathrm{pp}}+\tau_{\mathrm{ph,d}}+\tau_{\mathrm{ph,cr}}. \tag{5}$$

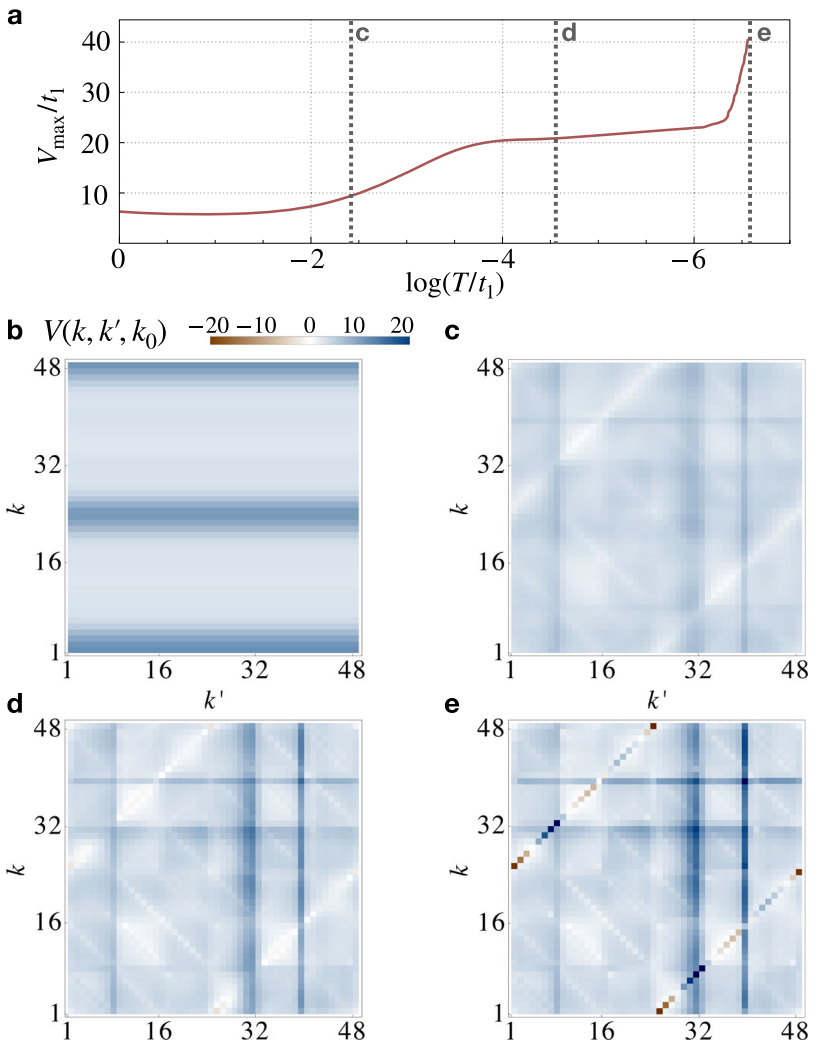

Fig. 6 Flow of the effective interaction. a Representative scale-dependence of the maximal value of the effective interaction $V_{max} = \max V(\mathbf{k}_1, \mathbf{k}_2, \mathbf{k}_3, \mathbf{k}_4)$ in the parameter region of the $g + ig$ SC instability. During the different stages of the RG flow, the different interaction channels (i.e. the pp-channel and the ph-channels) contribute. The initial increase of V_{max} for $\log T/t \gtrsim -4$ is driven by the particle-hole fluctuations. Sufficiently far away from nesting, these fluctuations are not critical, i.e. V_{max} nearly saturates (cf. plateau for $-4 \gtrsim \log T/t \gtrsim -6$). Eventually, particle-particle fluctuations lead to a divergence of the flow. **b** Interaction V with conventions as described in Fig. 2b for $T = T_0$. **c**–**e** Interaction V for the three choices of T as indicated in panel (**a**), exhibiting different dominant features. The strongest vertical and horizontal features in c,d correspond to valley fluctuations with momentum transfer of $\mathbf{k}_1 - \mathbf{k}_3 = \mathbf{Q}_\alpha$ and $\mathbf{k}_2 - \mathbf{k}_3 = \mathbf{Q}_\alpha$ ($\alpha = 1, 2, 3$), diagonal features in e are typical for superconductivity with $\mathbf{k}_1 + \mathbf{k}_2 = \mathbf{k}_3 + \mathbf{k}_4 = 0$.

with contributions from the particle-particle (pp), the direct paricle-hole (ph,d), and the crossed particle-hole (ph,cr) channel on the right hand side. The corresponding diagrams are visualized in Fig. 4. They are given by

$$\tau_{pp} = -\frac{1}{2}\int_{BZ} d^2k V(\mathbf{k}_1, \mathbf{k}_2, \mathbf{k}) L(\mathbf{k}, \mathbf{q}_{pp}) V(\mathbf{k}, \mathbf{q}_{pp}, \mathbf{k}_3), \tag{6}$$

where we used the short hand $\int_{BZ} d^2k = -A_{BZ}^{-1} \int d^2k$ and A_{BZ} is the area of the Brillouin zone. The particle-hole contributions read

$$\begin{aligned}\tau_{ph,d} = \tfrac{1}{2}\int_{BZ} d^2k [&2V(\mathbf{k}_1, \mathbf{k}, \mathbf{k}_3) L(\mathbf{k}, \mathbf{q}_d) V(\mathbf{q}_d, \mathbf{k}_2, \mathbf{k}) \\ &- V(\mathbf{k}, \mathbf{k}_1, \mathbf{k}_3) L(\mathbf{k}, \mathbf{q}_d) V(\mathbf{q}_d, \mathbf{k}_2, \mathbf{k}) \\ &- V(\mathbf{k}, \mathbf{k}_1, \mathbf{k}_3) L(\mathbf{k}, \mathbf{q}_d) V(\mathbf{k}_2, \mathbf{q}_d, \mathbf{k})],\end{aligned} \tag{7}$$

and

$$\tau_{ph,cr} = -\frac{1}{2}\int_{BZ} d^2k V(\mathbf{k}, \mathbf{k}_2, \mathbf{k}_3) L(\mathbf{k}, \mathbf{q}_{cr}) V(\mathbf{k}_1, \mathbf{q}_{cr}, \mathbf{k}). \tag{8}$$

In these expressions, we introduced $\mathbf{q}_{pp} = -\mathbf{k} + \mathbf{k}_1 + \mathbf{k}_2$, $\mathbf{q}_d = \mathbf{k} + \mathbf{k}_1 - \mathbf{k}_3$, $\mathbf{q}_{cr} = \mathbf{k} + \mathbf{k}_2 - \mathbf{k}_3$, and the loop kernel

$$L(\mathbf{k}, \pm\mathbf{k} + \mathbf{k}') = \frac{d}{dT}\left[T \sum_{i\omega} G_0(i\omega, \mathbf{k}) G_0(\pm i\omega, \pm\mathbf{k} + \mathbf{k}')\right], \tag{9}$$

with the free propagator $G_0(i\omega, \mathbf{k}) = [i\omega - \xi_{\mathbf{k}}]^{-1}$. In these expressions, we have neglected the (external) frequency dependence assuming that the strongest correlations occur for the lowest Matsubara frequencies.

For the numerical implementation, we resolve the momentum dependence in a so-called patching scheme that divides the Fermi surface into N pieces based on equidistant angles and treats the radial dependence for a fixed angle as constant. This accurately describes the relevant momentum dependence, which is along the Fermi surface. In our numerical calculations, we have chosen between $N = 48$ and $N = 96$ patches, cf. Fig. 1b.

Our results on the type of instability do not depend on this choice and the quantitative results for critical temperatures vary only mildly with N.

The initial condition for $V(\mathbf{k}_1, \mathbf{k}_2, \mathbf{k}_3)$ at high temperatures is given by the Fourier transform of H_I in Eq. (2). We set $T_0 = \max(\epsilon_{\mathbf{k}})$ as starting temperature. We then calculate the temperature evolution of $V(\mathbf{k}_1, \mathbf{k}_2, \mathbf{k}_3)$ according to Eq. (5) by solving the integro-differential equation. As described above, the development of strong correlations is signaled by a diverging $V(\mathbf{k}_1, \mathbf{k}_2, \mathbf{k}_3)$ at a critical temperature T_c. Our numerical criterion to detect the divergence is a convex temperature dependence and $\max[V(\mathbf{k}_1, \mathbf{k}_2, \mathbf{k}_3)]$ exceeding $30t_1$. T_c would be the mean-field critical temperature in an RPA resummation, however, here the estimate is slightly improved due to the inclusion of the coupling between different channels. The Fermi liquid is stable within our numerical accuracy if no divergence occurs before $T_l = 2 \cdot 10^{-4} t_1$ is reached. In the cases when correlated states develop, we can read off the type of correlations from the momentum structure of $V(\mathbf{k}_1, \mathbf{k}_2, \mathbf{k}_3)$ at T_c. Up to an overall constant, this determines the effective interaction close to the instability and directly suggests the order-parameter corresponding to the instability. Following this procedure for an extended range of parameters, we obtain the presented phase diagrams. We have also checked that the qualitative features of the phase diagrams remain the same when we vary the overall interaction strength U. We show examples for $U = 3t_1$ and $U = 5t_1$ in Fig. 5.

An advantage of the FRG approach over other methods such as mean-field or the random phase approximation is that it takes the coupling between different ordering channels into account on equal footing. In particular, it can resolve the generation of an attraction in the pairing channel due to particle-hole fluctuations. In this way the bosons mediating the pairing can be read off in an unbiased way, i.e. without choosing specific channels as relevant by hand. In our case, fluctuations due to nesting increase the interaction in the particle-hole channel via $\tau_{\mathrm{ph,d/cr}}$ upon lowering the temperature (ph diagrams in Fig. 4), which then feed back into the pairing channel via τ_{pp} (pp diagram in Fig. 4) and yield the effective pairing interaction shown in Fig. 2b. This can be visualized by snapshots of the interaction during the flow (Fig. 6), which first develops horizontal features typical for particle-hole fluctuations with momentum transfer Q_α and which are associated with the VDW instability, Eventually, diagonal features of the effective interaction are induced that correspond to the superconducting pairing instability.

Landau functional

To extract the form factors of the superconducting instabilities, we diagonalize $V(\mathbf{k}, -\mathbf{k}, \mathbf{k}')$, keep the eigenfunction(s) with the largest eigenvalue and approximate it by lattice harmonics so that $V(\mathbf{k}, -\mathbf{k}, \mathbf{k}') \approx -\lambda \sum_{i=1,2} \int d\mathbf{k} d\mathbf{k}' g_i(\mathbf{k}) g_i(\mathbf{k}') c^\dagger_{\mathbf{k}'+} c^\dagger_{-\mathbf{k}'-} c_{-\mathbf{k}-} c_{\mathbf{k}+}$ with $\lambda > 0$. We have used the extracted lattice harmonics to derive the Landau functional (3) from our microscopic model. The decisive prefactor of the term $|\Delta_1^2 + \Delta_2^2|^2$ is given by

$$\begin{aligned}\gamma &= T \sum_{i\omega} \int_{\mathrm{BZ}} d^2k \frac{g_1(\mathbf{k})^2 g_2(\mathbf{k})^2}{(i\omega - \xi_{\mathbf{k}})^2 (i\omega + \xi_{\mathbf{k}})^2} \\ &= \int_{\mathrm{BZ}} d^2k \, g_1(\mathbf{k})^2 g_2(\mathbf{k})^2 \frac{1 - 2n_F(\xi_{\mathbf{k}}) + 2\xi_{\mathbf{k}} n_F'(\xi_{\mathbf{k}})}{4\xi_{\mathbf{k}}^3}\end{aligned} \tag{10}$$

with the Fermi function n_F. We have calculated γ numerically and found it to be positive in the considered range of μ and T. As an analytical estimate for γ, we can approximate the dispersion by $\xi \approx k^2/(2m) - \mu$ with density of states ρ_ϵ, and the form factors by $g_1 = \cos(n\varphi)$, $g_2 = \sin(n\varphi)$ with $\varphi = \arctan k_y/k_x$ and $n = 4$ for $g + ig$ superconductivity ($n = 2$ for $d + id$ and $n = 1$ for $p + ip$). With this simplification, we obtain

$$\begin{aligned}\gamma &\approx \int d\varphi \cos^2(n\varphi) \sin^2(n\varphi) \int d\epsilon \rho_\epsilon \frac{\frac{1}{2} - n_F(\epsilon) + \epsilon n_F'(\epsilon)}{2\epsilon^3} \\ &= \frac{m}{16\pi T^2} \int \frac{\sinh(x) - x}{4x^3(1 + \cosh(x))} \approx 0.05 \frac{m}{16\pi T^2},\end{aligned} \tag{11}$$

which we can take as a rough estimate for γ if μ is away from the Van Hove energy. Right at the Van Hove energy, an additional logarithmic dependence on T_c emerges.

DATA AVAILABILITY

Data and simulation codes are available from the corresponding authors upon reasonable request.

Received: 22 April 2022; Accepted: 30 August 2022;
Published online: 04 October 2022

REFERENCES

1. Hofmann, J. S., Chowdhury, D., Kivelson, S. A. & Berg, E. Superconductivity is boundless. *arXiv preprint arXiv:2105.09322*. https://arxiv.org/abs/2105.09322 (2021).
2. Lilia, B. et al. The 2021 room-temperature superconductivity roadmap. *J. Phys. Condens. Matter* **34**, 183002 (2022).
3. Stewart, G. R. Unconventional superconductivity. *Adv. Phys.* **66**, 75–196 (2017).
4. Nayak, C., Simon, S. H., Stern, A., Freedman, M. & Das Sarma, S. Non-abelian anyons and topological quantum computation. *Rev. Mod. Phys.* **80**, 1083–1159 (2008).
5. Joynt, R. & Taillefer, L. The superconducting phases of UPt_3. *Rev. Mod. Phys.* **74**, 235–294 (2002).
6. Avers, K. E. et al. Broken time-reversal symmetry in the topological superconductor UPt_3. *Nat. Phys.* **16**, 531–535 (2020).
7. Jiao, L. et al. Chiral superconductivity in heavy-fermion metal UTe_2. *Nature* **579**, 523–527 (2020).
8. Zhang, P. et al. Observation of topological superconductivity on the surface of an iron-based superconductor. *Science* **360**, 182–186 (2018).
9. Li, Y. et al. Electronic properties of the bulk and surface states of $Fe_{1+y}Te_{1-x}Se_x$. *Nat. Mater.* https://doi.org/10.1038/s41563-021-00984-7 (2021).
10. Cao, Y. et al. Unconventional superconductivity in magic-angle graphene superlattices. *Nature* **556**, 43–50 (2018).
11. Cao, Y. et al. Correlated insulator behaviour at half-filling in magic-angle graphene superlattices. *Nature* **556**, 80–84 (2018).
12. Yankowitz, M. et al. Tuning superconductivity in twisted bilayer graphene. *Science* **363**, 1059–1064 (2019).
13. Kerelsky, A. et al. Maximized electron interactions at the magic angle in twisted bilayer graphene. *Nature* **572**, 95–100 (2019).
14. Sharpe, A. L. et al. Emergent ferromagnetism near three-quarters filling in twisted bilayer graphene. *Science* **365**, 605–608 (2019).
15. Lu, X. et al. Superconductors, orbital magnets and correlated states in magic-angle bilayer graphene. *Nature* **574**, 20–23 (2019).
16. Serlin, M. et al. Intrinsic quantized anomalous Hall effect in a moiré heterostructure. *Science* **367**, 900–903 (2020).
17. Kennes, D. M. et al. Moiré heterostructures as a condensed-matter quantum simulator. *Nat. Phys.* **17**, 155–163 (2021).
18. Liu, X. et al. Tunable spin-polarized correlated states in twisted double bilayer graphene. *Nature* **583**, 221–225 (2020).
19. Cao, Y. et al. Tunable correlated states and spin-polarized phases in twisted bilayer–bilayer graphene. *Nature* **583**, 215–220 (2020).
20. Shen, C. et al. Correlated states in twisted double bilayer graphene. *Nat. Phys.* **16**, 520–525 (2020).
21. Chen, G. et al. Evidence of a gate-tunable Mott insulator in a trilayer graphene moiré superlattice. *Nat. Phys.* **15**, 237–241 (2019).
22. Chen, G. et al. Signatures of tunable superconductivity in a trilayer graphene moiré superlattice. *Nature* **572**, 215–219 (2019).
23. Chen, G. et al. Tunable correlated chern insulator and ferromagnetism in a moiré superlattice. *Nature* **579**, 56–61 (2020).
24. Burg, G. W. et al. Correlated insulating states in twisted double bilayer graphene. *Phys. Rev. Lett.* **123**, 197702 (2019).
25. Rubio-Verdú, C. et al. Universal moiré nematic phase in twisted graphitic systems. *arXiv:2009.11645*. https://arxiv.org/abs/2009.11645 (2020).

26. Xian, L., Kennes, D. M., Tancogne-Dejean, N., Altarelli, M. & Rubio, A. Multiflat bands and strong correlations in twisted bilayer boron nitride: Doping-induced correlated insulator and superconductor. *Nano Lett.* **19**, 4934–4940 (2019).
27. Lian, B., Liu, Z., Zhang, Y. & Wang, J. Flat Chern band from twisted bilayer $MnBi_2Te_4$. *Phys. Rev. Lett.* **124**, 126402 (2020).
28. Kennes, D. M., Xian, L., Claassen, M. & Rubio, A. One-dimensional flat bands in twisted bilayer germanium selenide. *Nat. Commun.* **11**, 1124 (2020).
29. Tang, Y. et al. Simulation of Hubbard model physics in WSe_2/WS_2 moiré superlattices. *Nature* **579**, 353–358 (2020).
30. Regan, E. C. et al. Mott and generalized Wigner crystal states in WSe_2/WS_2 moiré superlattices. *Nature* **579**, 359–363 (2020).
31. Jin, C. et al. Stripe phases in WSe_2/WS_2 moiré superlattices. *Nat. Mater.* **20**, 940–944 (2021).
32. Li, T. et al. Quantum anomalous hall effect from intertwined moiré bands. *Nature* **600**, 641–646 (2021).
33. Wang, L. et al. Correlated electronic phases in twisted bilayer transition metal dichalcogenides. *Nat. Mater.* **19**, 861–866 (2020).
34. Wu, F., Lovorn, T., Tutuc, E. & Macdonald, A. H. Hubbard model physics in transition metal dichalcogenide moiré bands. *Phys. Rev. Lett.* **121**, 26402 (2018).
35. Wu, F., Lovorn, T., Tutuc, E., Martin, I. & Macdonald, A. H. Topological insulators in twisted transition metal dichalcogenide homobilayers. *Phys. Rev. Lett.* **122**, 86402 (2019).
36. Naik, M. H. & Jain, M. Ultraflat bands and shear solitons in moiré patterns of twisted bilayer transition metal dichalcogenides. *Phys. Rev. Lett.* **121**, 266401 (2018).
37. Ruiz-Tijerina, D. A. & Fal'ko, V. I. Interlayer hybridization and moiré superlattice minibands for electrons and excitons in heterobilayers of transition-metal dichalcogenides. *Phys. Rev. B* **99**, 125424 (2019).
38. Schrade, C. & Fu, L. Spin-valley density wave in moiré materials. *Phys. Rev. B* **100**, 035413 (2019).
39. Zhou, Y., Sheng, D. N. & Kim, E.-A. Quantum phases of transition metal dichalcogenide moiré systems. *Phys. Rev. Lett.* **128**, 157602 (2022).
40. Jin, C. et al. Observation of moiré excitons in WSe_2/WS_2 heterostructure superlattices. *Nature* **567**, 76–80 (2019).
41. Wang, Z. et al. Evidence of high-temperature exciton condensation in two-dimensional atomic double layers. *Nature* **574**, 76–80 (2019).
42. Shimazaki, Y. et al. Strongly correlated electrons and hybrid excitons in a moiré heterostructure. *Nature* **580**, 472–477 (2020).
43. Morales-Durán, N., Hu, N. C., Potasz, P. & MacDonald, A. H. Nonlocal interactions in moiré Hubbard systems. *Phys. Rev. Lett.* **128**, 217202 (2022).
44. Metzner, W., Salmhofer, M., Honerkamp, C., Meden, V. & Schönhammer, K. Functional renormalization group approach to correlated fermion systems. *Rev. Mod. Phys.* **84**, 299–352 (2012).
45. Platt, C., Hanke, W. & Thomale, R. Functional renormalization group for multi-orbital Fermi surface instabilities. *Adv. Phys.* **62**, 453–562 (2013).
46. Scherer, M. M. et al. Excitonic instability and unconventional pairing in the nodal-line materials ZrSiS and ZrSiSe. *Phys. Rev. B* **98**, 241112 (2018).
47. Wolf, S., Di Sante, D., Schwemmer, T., Thomale, R. & Rachel, S. Triplet superconductivity from nonlocal Coulomb repulsion in an atomic Sn layer deposited onto a Si(111) substrate. *Phys. Rev. Lett.* **128**, 167002 (2022).
48. Klebl, L., Fischer, A., Classen, L., Scherer, M. M. & Kennes, D. M. Competition of density waves and superconductivity in twisted tungsten diselenide. *arXiv preprint arXiv:2204.00648*. https://arxiv.org/abs/2204.00648 (2022).
49. Dupuis, N. et al. The nonperturbative functional renormalization group and its applications. *Phys. Rep.* **910**, 1–114 (2021).
50. Nandkishore, R., Chern, G.-W. & Chubukov, A. V. Itinerant half-metal spin-density-wave state on the hexagonal lattice. *Phys. Rev. Lett.* **108**, 227204 (2012).
51. Martin, I. & Batista, C. D. Itinerant electron-driven chiral magnetic ordering and spontaneous quantum Hall effect in triangular lattice models. *Phys. Rev. Lett.* **101**, 156402 (2008).
52. Nandkishore, R., Thomale, R. & Chubukov, A. V. Superconductivity from weak repulsion in hexagonal lattice systems. *Phys. Rev. B* **89**, 144501 (2014).
53. Honerkamp, C. Instabilities of interacting electrons on the triangular lattice. *Phys. Rev. B* **68**, 104510 (2003).
54. Sigrist, M. & Ueda, K. Phenomenological theory of unconventional superconductivity. *Rev. Mod. Phys.* **63**, 239–311 (1991).
55. Volovik, G. E. On edge states in superconductors with time inversion symmetry breaking. *JETP Lett.* **66**, 522–527 (1997).
56. Read, N. & Green, D. Paired states of fermions in two dimensions with breaking of parity and time-reversal symmetries and the fractional quantum hall effect. *Phys. Rev. B* **61**, 10267–10297 (2000).
57. Black-Schaffer, A. M. & Honerkamp, C. Chiral *d*-wave superconductivity in doped graphene. *J. Phys. Condens. Matter* **26**, 423201 (2014).
58. Senthil, T., Marston, J. B. & Fisher, M. P. A. Spin quantum Hall effect in unconventional superconductors. *Phys. Rev. B* **60**, 4245–4254 (1999).
59. Horovitz, B. & Golub, A. Superconductors with broken time-reversal symmetry: Spontaneous magnetization and quantum Hall effects. *Phys. Rev. B* **68**, 214503 (2003).
60. Kiesel, M. L., Platt, C., Hanke, W., Abanin, D. A. & Thomale, R. Competing many-body instabilities and unconventional superconductivity in graphene. *Phys. Rev. B* **86**, 020507 (2012).
61. Nandkishore, R., Levitov, L. & Chubukov, A. Chiral superconductivity from repulsive interactions in doped graphene. *Nat. Phys.* **8**, 158 (2012).
62. Kennes, D. M., Lischner, J. & Karrasch, C. Strong correlations and $d+id$ superconductivity in twisted bilayer graphene. *Phys. Rev. B* **98**, 241407 (2018).
63. Classen, L., Chubukov, A. V., Honerkamp, C. & Scherer, M. M. Competing orders at higher-order Van Hove points. *Phys. Rev. B* **102**, 125141 (2020).
64. Zhou, S. & Wang, Z. Nodal $d+id$ pairing and topological phases on the triangular lattice of $Na_xCoO_2 \cdot yH_2O$: evidence for an unconventional superconducting state. *Phys. Rev. Lett.* **100**, 217002 (2008).
65. Kiesel, M. L., Platt, C., Hanke, W. & Thomale, R. Model evidence of an anisotropic chiral $d+id$-wave pairing state for the water-intercalated $Na_xCoO_2 \cdot y\mathbf{H_2O}$ superconductor. *Phys. Rev. Lett.* **111**, 097001 (2013).
66. Halbertal, D. et al. Moiré metrology of energy landscapes in van der waals heterostructures. *Nat. Commun.* **12**, 242 (2021).
67. Black-Schaffer, A. M. Edge properties and Majorana fermions in the proposed chiral *d*-wave superconducting state of doped graphene. *Phys. Rev. Lett.* **109**, 197001 (2012).
68. Löthman, T. & Black-Schaffer, A. M. Defects in the $d+id$-wave superconducting state in heavily doped graphene. *Phys. Rev. B* **90**, 224504 (2014).
69. Enaldiev, V. V., Zólyomi, V., Yelgel, C., Magorrian, S. J. & Fal'ko, V. I. Stacking domains and dislocation networks in marginally twisted bilayers of transition metal dichalcogenides. *Phys. Rev. Lett.* **124**, 206101 (2020).
70. Weston, A. et al. Atomic reconstruction in twisted bilayers of transition metal dichalcogenides. *Nat. Nanotechnol.* **15**, 592–597 (2020).
71. Zhang, C. et al. Interlayer couplings, moiré patterns, and 2D electronic superlattices in MoS2/WSe2 hetero-bilayers. *Sci. Adv.* **3**, e1601459 (2017).
72. Hauck, J. B., Honerkamp, C., Achilles, S. & Kennes, D. M. Electronic instabilities in Penrose quasicrystals: Competition, coexistence, and collaboration of order. *Phys. Rev. Res.* **3**, 023180 (2021).
73. Keldysh, L. V. Coulomb interaction in thin semiconductor and semimetal films. *JETP Lett.* **29**, 658 (1979).
74. Jiang, Y., Yao, D.-X., Carlson, E. W., Chen, H.-D. & Hu, J. Andreev conductance in the $d+id'$ -wave superconducting states of graphene. *Phys. Rev. B* **77**, 235420 (2008).
75. Lu, H.-Y. et al. Electronic raman spectra in superconducting graphene: a probe of the pairing symmetry. *Phys. Rev. B* **88**, 085416 (2013).

ACKNOWLEDGEMENTS

We thank Andrey Chubukov and Abhay Pasupathy for useful discussions. M.M.S. acknowledges support by the Deutsche Forschungsgemeinschaft (DFG, German Research Foundation) through SFB 1238 (project C02, project id 277146847) and the DFG Heisenberg programme (project id 452976698). D.M.K. acknowledges support from the DFG through RTG 1995, within the Priority Program SPP 2244 "2DMP", under Germany's Excellence Strategy-Cluster of Excellence Matter and Light for Quantum Computing (ML4Q) EXC2004/1 - 390534769, and from the Max Planck-New York City Center for Non-Equilibrium Quantum Phenomena. L.C. was supported by the U.S. Department of Energy (DOE), Office of Basic Energy Sciences, under Contract No. DE-SC0012704. We acknowledge support by the Open Access Publication Funds of the Ruhr-Universität Bochum.

AUTHOR CONTRIBUTIONS

The work was conceived by L.C. and M.M.S. M.M.S. computed functional RG data. All authors analyzed and interpreted the results and wrote the manuscript.

FUNDING

Open Access funding enabled and organized by Projekt DEAL.

COMPETING INTERESTS

The authors declare no competing interests.

ADDITIONAL INFORMATION

Correspondence and requests for materials should be addressed to Michael M. Scherer.

Reprints and permission information is available at http://www.nature.com/reprints

Publisher's note Springer Nature remains neutral with regard to jurisdictional claims in published maps and institutional affiliations.